

# Rhodopsin Absorption from First Principles: Bypassing Common Pitfalls

Omar Valsson,<sup>†</sup> Pablo Campomanes,<sup>‡</sup> Ivano Tavernelli,<sup>‡</sup> Ursula Rothlisberger,<sup>\*,‡</sup> and Claudia Filippi<sup>\*,†</sup>

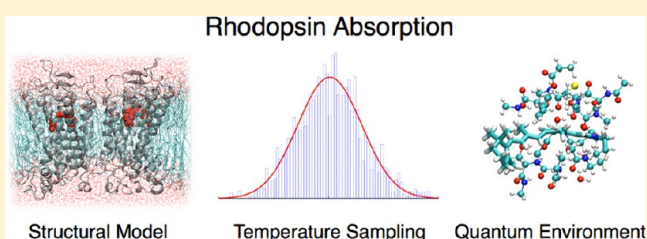
<sup>†</sup>MESA+ Institute for Nanotechnology, University of Twente, P.O. Box 217, 7500 AE Enschede, The Netherlands

<sup>‡</sup>Laboratory of Computational Chemistry and Biochemistry, Ecole Polytechnique Fédérale de Lausanne (EPFL), CH-1015 Lausanne, Switzerland

## S Supporting Information

**ABSTRACT:** Bovine rhodopsin is the most extensively studied retinal protein and is considered the prototype of this important class of photosensitive biosystems involved in the process of vision. Many theoretical investigations have attempted to elucidate the role of the protein matrix in modulating the absorption of retinal chromophore in rhodopsin, but, while generally agreeing in predicting the correct location of the absorption maximum, they often reached contradicting conclusions on how the environment

tunes the spectrum. To address this controversial issue, we combine here a thorough structural and dynamical characterization of rhodopsin with a careful validation of its excited-state properties via the use of a wide range of state-of-the-art quantum chemical approaches including various flavors of time-dependent density functional theory (TDDFT), different multireference perturbative schemes (CASPT2 and NEVPT2), and quantum Monte Carlo (QMC) methods. Through extensive quantum mechanical/molecular mechanical (QM/MM) molecular dynamics simulations, we obtain a comprehensive structural description of the chromophore–protein system and sample a wide range of thermally accessible configurations. We show that, in order to obtain reliable excitation properties, it is crucial to employ a sufficient number of representative configurations of the system. In fact, the common use of a single, ad hoc structure can easily lead to an incorrect model and an agreement with experimental absorption spectra due to cancelation of errors. Finally, we show that, to properly account for polarization effects on the chromophore and to quench the large blue-shift induced by the counterion on the excitation energies, it is necessary to adopt an enhanced description of the protein environment as given by a large quantum region including as many as 250 atoms.



## 1. INTRODUCTION

Rhodopsin<sup>1,2</sup> is the visual pigment responsible for dim light vision and is the most extensively studied member of the family of visual opsin proteins, a large class of G-protein-coupled receptors that respond to light and initiate the visual transduction process in vertebrate.<sup>3,4</sup> Most visual opsins share the same covalently linked chromophore, the retinal protonated Schiff base (RPSB) molecule, while variations in the chromophore–protein interaction tune the absorption maximum over a very wide range of wavelengths from 420 to 570 nm.<sup>3,4</sup> This remarkable spectral tuning has prompted a large number of experimental<sup>1–32</sup> and theoretical<sup>32–62</sup> studies that have attempted to understand the molecular mechanism underlying the functioning of visual opsins.

Due to the complexity of these systems, obtaining an accurate theoretical description of the absorption in visual opsins is not a trivial task which might depend on various ingredients entering in the calculations (e.g., the method chosen to optimize the structure or to compute the excited states, the protonation states of relevant amino acids, etc.). Nevertheless, for rhodopsin, many theoretical studies have reported a remarkable agreement with the experimental absorption maximum even though these studies often differ considerably in the theoretical approaches employed

and normally resort to different approximations in the treatment of the chromophore–protein interaction. However, in spite of the generally good agreement in the absorption wavelengths, different studies often lead to very varying conclusions as regards the role of the protein environment in tuning the excitation energy of the chromophore. In particular, while there is general consensus that the addition of the counterion induces a blue-shift in the excitation energy of retinal, the magnitude of the predicted shift spans a range as large as 0.3–1.2 eV.<sup>35–40,55–61</sup> Furthermore, even more controversial is the issue of whether the rest of the protein environment quenches the effect of the counterion. Several studies<sup>35,37–40</sup> find that adding the rest of protein residues has a negligible effect (0.01–0.1 eV), while others<sup>36,55–61</sup> observe a red-shift which can be as large as 1.2 eV and cancel the blue-shift induced by the counterion. Remarkably, all studies agree in reporting a final excitation energy which lies within 0.1 eV of the experimental absorption maximum at 498 nm (2.49 eV).<sup>5</sup> It is clear that the messages conveyed by these contradicting studies cannot all be simultaneously right.

**Received:** November 28, 2012

**Published:** March 13, 2013



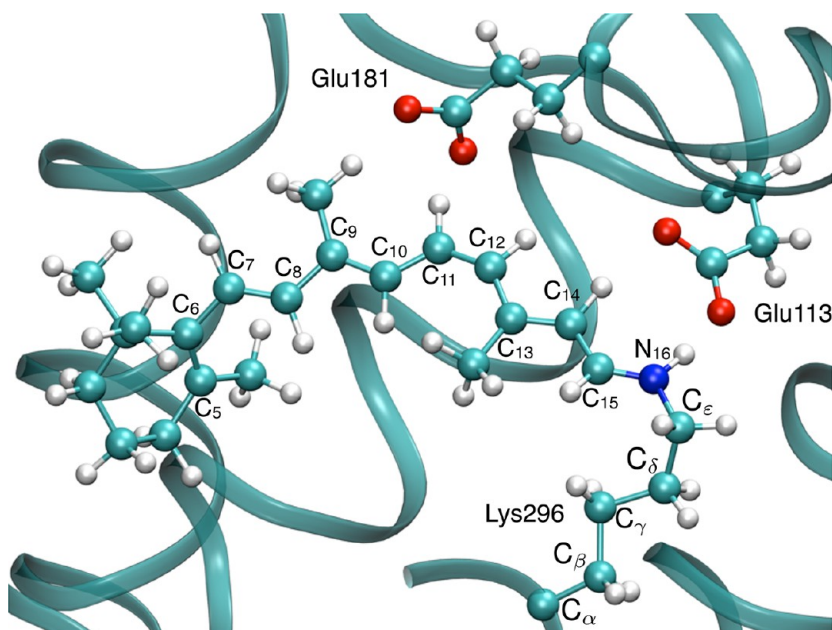


**Figure 1.** The retinal protonated Schiff base (RPSB) with the Glu113 counterion and Glu181. We also show the labeling used for the conjugated chain of the RPSB and the side chain of the Lys296 residue.

Therefore, the apparent agreement with experiment is in most cases due to a favorable cancelation of errors.

Despite the numerous theoretical investigations, it remains therefore unclear whether we are in a position to accurately describe the optical properties of opsins from first principles and whether we have identified all necessary ingredients to achieve this goal. It is clear that one should use an accurate approach to compute the electronic excitations, but, even if we restrict ourselves to highly correlated methods, this choice is far from obvious as the various techniques yield very different results even for the retinal chromophore in gas phase.<sup>63–67</sup> Furthermore, for the description of the chromophore–protein interaction, it has been pointed out that, to obtain accurate absorption energies, the mutual polarization of the chromophore and the protein environment should be considered.<sup>45–47</sup> Nevertheless, the generally accepted procedure is to employ a standard embedding scheme, where only the chromophore is described at the quantum level, while the rest of the protein environment is modeled by employing fixed, partial point charges, normally taken from a particular classical force field. In this multiscale scheme, the point charges polarize the quantum chromophore in its ground and excited states, whereas the environment does not respond to the presence of the chromophore. Finally, another important aspect of modeling photoactive proteins is to properly account for the dynamical nature of the protein since thermal fluctuations can affect the structure, the chromophore–protein interaction, and the resulting excitation energy. This point has been largely ignored in most previous theoretical studies, which just consider a single, static model of the protein. In such models, the protein is often taken to be the available crystallographic structure, where only the chromophore or a small region around it is relaxed, while the rest of the protein is kept fixed at the crystallographic positions. The investigations which attempt to include thermal sampling do so in a limited way, either by only performing classical molecular dynamics (MD) followed by QM/MM geometrical optimization<sup>49–51</sup> or by performing QM/MM MD in which often a part of the protein is kept fixed.<sup>52–54</sup>

Here, we will explore these issues to understand which theoretical ingredients are needed for an accurate description of the optical properties of rhodopsin. To achieve this goal, we employ a realistic model of rhodopsin embedded in its native membrane environment, which was carefully equilibrated for 300 ns with classical MD.<sup>68</sup> For this model system, we perform extensive and fully unconstrained QM/MM MD simulations of up to 18 ps length employing density functional theory (DFT) for the quantum part in order to obtain an accurate structural description of the chromophore and of the thermal fluctuations of the chromophore–protein system at room temperature. A thermally averaged absorption spectrum obtained with an expedient but more approximate approach such as the ZINDO method allows us to select a set of configurations close to the corresponding theoretical absorption band maximum, for which we recompute the excitation energies at a higher level of theory. In this step, we employ a range of highly correlated methods such as the quantum Monte Carlo (QMC), multireference perturbation theory (CASPT2), and the *n*-electron valence state perturbation theory (NEVPT2) approaches, to compute the excitation energies and systematically validate the use of certain flavors of TDDFT (in particular, CAM-B3LYP) in rhodopsin. Furthermore, with the use of enlarged quantum regions with as many as 250 atoms, we will explore at the TDDFT level whether the conventional point-charges embedding scheme based on a nonpolarizable classical force field properly accounts for the effect of the protein environment. Finally, we will compare our results with previous theoretical studies on rhodopsin<sup>55–61</sup> based on a QM/MM partial structure relaxation at the complete-active-space self-consistent-field level, combined with the original formulation<sup>69</sup> of CASPT2 to compute the excitation energies, and provide some reasons for the remarkable, but fortuitous, agreement with experiments achieved in these previous studies.

## 2. MODEL SYSTEM

Our model system of the bovine rhodopsin dark state in its adapted form consists of two rhodopsin monomers embedded in



an explicit membrane. This model system was employed to investigate rhodopsin signal transduction in our previous study,<sup>68</sup> where it was extensively equilibrated at room temperature using classical MD.

Rhodopsin consists of 348 amino acid residues, and, in our model system, all potentially charged amino acids, including the C- and N-termini, are considered to be in their default protonation states at physiological pH (i.e., charged), except Asp83 and Glu122 that are assumed to be neutral in line with FTIR experiments.<sup>19</sup> The somewhat controversial protonation state of Glu181 is here chosen as charged in line with recent experimental and theoretical studies<sup>32,53</sup> and is further tested as described in detail below. Histidine residues are considered to be protonated either at the N<sub>δ</sub> position (His100, His211) or the N<sub>ε</sub> position (His65, His152, His195, His278). As shown in Figure 1, the retinal chromophore is covalently linked to the Lys296 residue via a protonated Schiff base linkage, which we collectively call the retinal protonated Schiff base (RPSB). Other notable features are a disulfide bond between the Cys110 and Cys187 residues and two palmitic acid residues, which act as membrane anchoring points, that are bound to Cys322 and Cys323.

As shown in Figure 2, the rhodopsin dimer is embedded in an explicit membrane modeled by 1-stearoyl-2-oleoyl-*sn*-glycero-3-

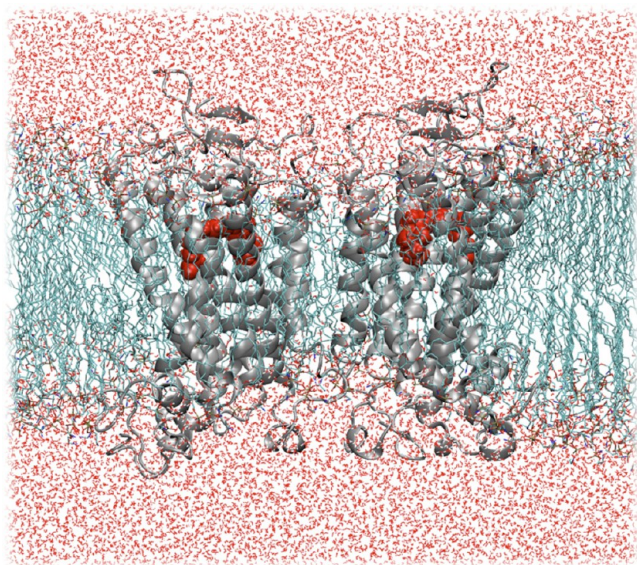
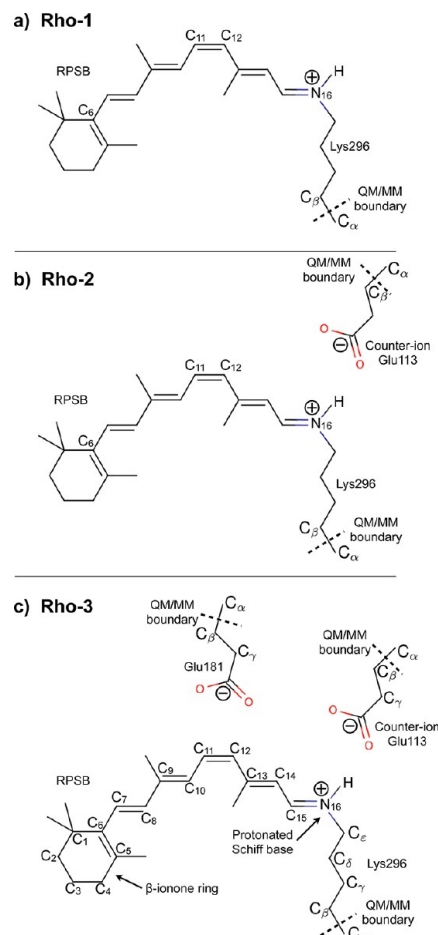


**Figure 2.** The rhodopsin dimer system used in the current work. The dimer is embedded in an explicit membrane, and the extracellular side is facing up. For clarity, hydrogens are not shown for the lipids.

phosphoethanolamine (SOPE) lipids, while explicit water molecules cover the cytoplasmic and extracellular sides. To obtain an overall neutral system, four sodium ions are added. The complete model system consists of the two rhodopsin monomers, approximately 20000 water molecules, and 300 lipids, which results in a total number of around 100000 atoms.

In the QM/MM MD simulations, we employ three different QM regions (see Chart 1): **Rho-1**, which only includes the retinal protonated Schiff base (RPSB); **Rho-2**, which includes the RPSB and the Glu113 counterion; and **Rho-3**, which includes the RPSB, the Glu113 counterion, and Glu181. In Chart 1c, we indicate the labeling used in this paper and the QM/MM boundaries employed in the QM/MM MD simulations.

**Chart 1. Three Different QM Regions Employed in the QM/MM MD Simulations: a) Rho-1, RPSB; b) Rho-2, RPSB + Glu113; c) Rho-3, RPSB + Glu113 + Glu181**



### 3. METHODS

**3.1. Molecular Dynamics. 3.1.1. Classical Simulations.** We give here the most relevant details of the classical MD setup and refer the reader to ref 68 for further details. The complete model system of the two rhodopsin monomers, the membrane, and the water molecules is placed in a periodically repeated cubic box with approximate dimensions of  $130 \times 80 \times 100 \text{ \AA}^3$ . The waters are described using the TIP3P force field,<sup>70</sup> and the AMBER/parm99 force field<sup>71</sup> is employed for all standard protein residues. The force fields for the RPSB and the palmitic acid residues are described in ref 72, while the AMBER/parm96 force field is used for the SOPE lipids. As described in ref 68, the entire system was equilibrated via classical MD for 300 ns in the NPT ensemble at a temperature of 300 K and a pressure of 1.05 bar.

**3.1.2. QM/MM Simulations.** In order to choose a representative starting structure for the QM/MM MD simulations, we perform a clustering analysis<sup>73</sup> on the last 100 ns of the classical MD equilibration run from ref 68. Each trajectory frame is ranked based on the number of neighboring frames that are within 1 Å RMSD cutoff. The top-ranked frame and all its neighboring frames then form a cluster. The frames corresponding to this cluster are then removed and the ranking process repeated until all frames are assigned to a given cluster. This results in a set of nonoverlapping clusters. We then use the central structure from the most populated cluster as a starting structure for our QM/MM MD simulations.

We perform the QM/MM MD simulations using the QM/MM scheme implemented in the CP2K package.<sup>74</sup> This QM/MM scheme employs the Quickstep QM code,<sup>75</sup> the Fict MM driver, and a real-space multigrid technique for the electrostatic coupling between the QM and MM regions.<sup>76,77</sup> The QM region is treated within density functional theory (DFT) in the generalized gradient approximation with the PBE<sup>78</sup> exchange-correlation functional, while the MM region is modeled using the AMBER force field described above. In the DFT calculations, a mixed Gaussian and plane waves (GPW) approach is used, where the wave function is described with a triple- $\zeta$  valence basis set augmented with two sets of polarization functions (TZV2P),<sup>79</sup> while the electron density is converged employing an auxiliary plane-wave basis set with a density cutoff of 320 Ry. The Goedecker-Teter-Hutter (GTH) pseudopotentials<sup>80,81</sup> are employed to describe the core electrons.

Only the chromophore located in one of the two monomers is included in the QM region, while the other, together with the rest of the protein environment, is treated at the MM level. As mentioned above, we perform three different QM/MM MD simulations that employ the different QM regions depicted in Chart 1: **Rho-1**, RPSB; **Rho-2**, RPSB and Glu113; **Rho-3**, RPSB, Glu113, and Glu181. As shown in Chart 1c, the QM/MM boundary for the Glu113 and Glu181 residues is through the  $C_\alpha$ – $C_\beta$  bond, while for the RPSB the boundary is through the  $C_\alpha$ – $C_\beta$  bond of Lys296. We saturate the valency of the QM regions by adding hydrogen capping atoms to the carbon QM atoms at the QM/MM boundary. In the QM/MM interface scheme used here,<sup>76</sup> the additional coordinates introduced by the hydrogen capping atoms are eliminated by employing the IMOMM<sup>82</sup> link-atom scheme where the positions of the hydrogen capping atoms are expressed as a function of the coordinates of the atoms forming the original bond, and the forces on the link atoms are accordingly redistributed. A scaling factor of 1.38 was applied to relate the MM carbon–carbon distances to the QM carbon–hydrogen ones. All simulations are performed in the Born–Oppenheimer (BOMD) approximation within the first-principles MD framework and with a time step of 0.5 fs. In each simulation, the QM region is initially optimized, while the MM part is kept frozen. The initial velocities after the optimization of the QM region are taken from a Maxwell–Boltzmann distribution at the specified temperature. The QM/MM MD simulations are then started and run in the canonical (NVT) ensemble for 15 ps with the **Rho-1** and **Rho-2** QM regions and 18 ps with **Rho-3**. A stochastic velocity rescaling thermostat<sup>83</sup> is employed to maintain the temperature at 300 K. To compute the geometrical averages and the ZINDO excitation energies, we discard the first part of the runs, corresponding to an equilibration time of about 7 ps, and use the last 7.5 ps, 7.3 ps, and 11.3 ps of the **Rho-1**, **Rho-2**, and **Rho-3** runs, respectively, where we collect frames every 5 fs (10 time steps) for a total number of 1491, 1450, and 2248 frames, respectively.<sup>84</sup>

**3.2. Static Excited-State Calculations.** **3.2.1. Theory Levels and Electronic Structure Codes.** For the ZINDO calculations, we employ the Gaussian 09 code<sup>85</sup> with the default settings and compute the excitation energies of the four lowest roots, which we weight with the oscillator strength to calculate the ZINDO absorption spectra. The TDDFT calculations with CAM-B3LYP<sup>86</sup> and LC- $\omega$ PBE<sup>87,88</sup> functionals are performed using the Gaussian 09 code and the 6-31+G\* basis set. For the CC2 calculations, we use the TURBOMOLE code<sup>89</sup> where we employ the resolution-of-the-identity (RI) approximation,<sup>90</sup> the

ANO-L-VDZP<sup>91</sup> basis set, and the aug-cc-pVQZ auxiliary basis set.<sup>92,93</sup>

The CASPT2 calculations are performed with the MOLCAS<sup>94</sup> 7.2 code. Unless otherwise stated, we use the default IPEA zero-order Hamiltonian<sup>95</sup> and report the single-state (SS) CASPT2 values. We use a constant imaginary level shift<sup>96</sup> of 0.1 au and employ the ANO-L-VDZP basis set. For the CAS active space, we include all 12  $\pi$  electrons in the reference and test the use of 12 to 15 active  $\pi$  orbitals, resulting in a CAS(12,12) to CAS(12,15) expansion. We use a state-average (SA) CASSCF wave function with equal weights over either the two ( $S_0$  and  $S_1$ ) or three ( $S_0$ ,  $S_1$ , and  $S_2$ ) lowest-energy states.

For the NEVPT2 calculations, we use the strongly contracted (SC) variant<sup>97–99</sup> as implemented in the ORCA 2.8<sup>100,101</sup> code and use the same basis set and SA-CASSCF wave function as in the CASPT2 calculations. The DMC calculations are performed with the CHAMP<sup>102</sup> code. In all DMC calculations, we use a CAS(12,12) expansion, SA-CASSCF wave functions optimized over two states with equal weights, and pseudopotentials with the corresponding double- $\zeta$  basis set<sup>103</sup> and with added s and p diffuse functions on the heavy atoms.

We choose different basis sets for the TDDFT and PT2 calculations since, depending on the code, segmented or generally contracted basis sets can be more efficient, with MOLCAS being for instance optimized for generally contracted basis sets. As shown in Tables S2 and S3, the excitation energies computed with the 6-31+G\* and ANO-L-VDZP basis sets differ by at most 0.02 eV both at the TDDFT/CAM-B3LYP and CASPT2 level and are within 0.01 eV of the corresponding aug-ANO-L-VDZP values. For further details on the choice of basis set, CAS active space, and various issues related to the CASPT2, NEVPT2, and DMC calculations, we refer the reader to the SI.

**3.2.2. Point-Charges Embedding Scheme.** In the computation of the excitation energies, we perform single-point electrostatically embedded QM calculations, where the fixed, partial point charges of the MM region polarize the ground- and excited-state densities of the QM region. We employ two different QM regions, one including only the chromophore (RPSB) and the another including the chromophore and the Glu113 counterion (RPSB+Glu113). For the RPSB, the boundary of the QM region is chosen along the  $C_\gamma$ – $C_\delta$  bond of the Lys296 residue, and it is along the  $C_\alpha$ – $C_\beta$  bond for Glu113. The valency of this QM region is saturated by adding hydrogen capping atoms at the atoms on the boundary. The MM environment is modeled by employing partial AMBER force field point charges at the atomic positions. The TDDFT/MM, CC2/MM, and NEVPT2/MM calculations are performed by including the partial MM charges as point charges. In the CASPT2/MM calculations, we employ the ESPF<sup>104</sup> electrostatic coupling scheme implemented in Molcas to include the partial point charges. We note that the usage of the ESPF electrostatic coupling scheme in the MOLCAS calculations leads to deviations of less than 0.02 and 0.01 eV in the CASSCF/MM and CASPT2/MM excitation energies, respectively, compared to the use of normal point charges as also employed in the NEVPT2/MM calculations with ORCA. Therefore, any difference in the CASPT2/MM and NEVPT2/MM results is due to the differences in the correlated methods and not due to the different electrostatic coupling scheme employed. The QMC/MM calculations are performed using the electrostatic coupling scheme as in the QM/MM approach employed in the CPMD code.<sup>77</sup> In the single-point excited-state calculations performed using point-charges embedding, we turn off the point charges of a



small group of MM atoms at the QM boundary as precautionary measure against overpolarization of the QM region (see the SI for details). However, we note that overpolarization of the QM region is not an issue in the present excited-state calculations since setting the charges to zero yields excitation energies at the TDDFT/CAM-B3LYP and CASPT2 level that differ by only 0.01 eV from the values obtained retaining the original charges. For clarity, we stress again that we only set these charges to zero in the single-point excited-state calculations when using the point-charges embedding scheme and that the ground-state QM/MM MD simulations with CP2K are performed with the full MM charges and a QM/MM electrostatic coupling<sup>76,77</sup> that cures possible problems with overpolarization of the QM region.

## 4. RESULTS

**4.1. QM/MM MD Simulations.** As well-known, the time scales accessible in QM/MM MD simulations are orders of magnitude smaller than what is possible in classical MD simulations. This makes the selection of a starting point in a QM/MM MD simulation a critical issue as the initial structure must be representative of an average configuration of the system. In this work, we make this selection by using a clustering analysis on a 100 ns classical MD simulation to identify an initial structure. Starting from this selected structure, we perform three different QM/MM MD simulations at room temperature that differ in the QM region used: **Rho-1** has the minimal QM region of the RPSB, **Rho-2** adds the Glu113 counterion to the QM region, and **Rho-3** additionally includes the Glu181 residue in the QM region. The **Rho-1**, **Rho-2**, and **Rho-3** simulations are run for a total time of 15 to 18 ps, from which we use the last 7 to 11 ps for the analysis and calculations below.

All three QM/MM MD simulations show the same hydrogen bonding network (HBN) around the chromophore in the protein pocket, which is well preserved from the initial structure from the cluster analysis and stable throughout each simulation. The HBN can be divided into two parts, one around the Glu113 counterion and the other around Glu181. As shown in Figure 3a, the Glu113 counterion is hydrogen bonded to a crystallographic water, wat2b,<sup>16,17</sup> and to Thr94, which is a residue known to be important for the stability of the protein pocket.<sup>21,22</sup> In the HBN around Glu181 shown in Figure 3b, one oxygen of Glu181 is hydrogen bonded to Tyr191 and Tyr192, while the other oxygen is hydrogen bonded to Tyr268 and a crystallographic water molecule, wat2a.<sup>15–17</sup> This water molecule also forms a hydrogen bond to Ser186 and the backbone of Cys187. Finally, another water molecule bridges the Tyr191 and Tyr268 residues.

We consider the protonation state of Glu181 to be charged as recent experimental<sup>32</sup> and theoretical<sup>32,53</sup> evidence is mounting in support of this choice. We also note here that, throughout the 100 ns classical MD simulation, the RMSD of the residues around the active site pocket is low when compared with the initial X-ray structure, further confirming the internal consistency of our model and that the protonation states used, especially the one chosen for Glu181, are adequate. This is also in line with a previous classical MD study<sup>72</sup> on a rhodopsin monomer. Furthermore, to investigate the effect of the chosen protonation state of Glu181 on the absorption energy, we perform MD simulations of the E181Q mutant, which displays an experimental absorption maximum at 2.44 eV,<sup>31,32</sup> which is red-shifted by only 0.05 eV with respect to the absorption peak in native rhodopsin. We equilibrate E181Q at the QM/MM level at 300 K and then slowly anneal it down to 0 K. The excitation energies are then computed on the annealed structure of the

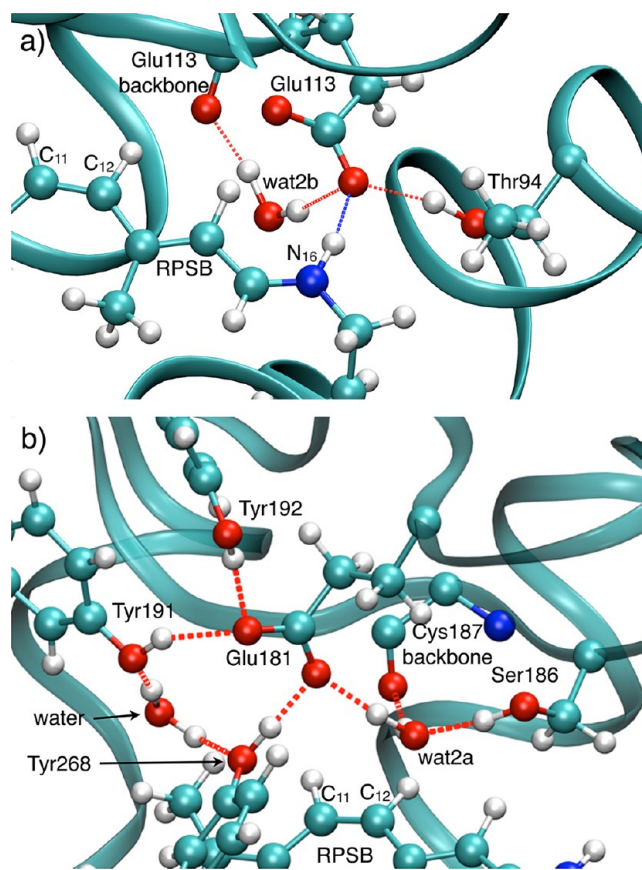


**Figure 3.** The hydrogen bonding network (HBN) around the chromophore in the protein pocket: a) HBN around the Glu113 counterion and b) HBN around Glu181.

E181Q mutant at the CAM-B3LYP and the CASPT2 level with a point-charges embedding scheme and compared to the corresponding energies obtained with a similarly annealed structure from the **Rho-1** trajectory of wildtype rhodopsin. In agreement with absorption experiments<sup>31,32</sup> and previous theoretical studies,<sup>32,53</sup> we do not observe a substantial difference in the value of the excitation energies (less than 0.02 eV), which indicates that the charge neutralization of Glu181 (through a E181Q mutation) does not significantly affect the absorption properties of rhodopsin.

In Table 1, we show the relevant geometrical parameters for the three QM/MM runs. For comparison, the geometrical parameters of the retinal chromophore optimized in the gas phase are presented in Table S1 in the SI. As observed in the crystallographic structures and expected from the location in the protein pocket, the geometry of the chromophore is considerably distorted by the interactions with the protein environment with respect to the gas-phase geometry. Interactions with the residues in the protein pocket significantly distort the conjugated chain of the chromophore from planarity, as can be seen from the C<sub>11</sub>–C<sub>12</sub> dihedral angle ( $\phi_{C10-C11-C12-C13}$ ). This is also observed in the overall length of the conjugated chain since the C<sub>6</sub>–N<sub>16</sub> distance ( $d_{C6-N16}$ ) is about 0.3–0.5 Å shorter than in the gas-phase geometry, indicating a more bent chromophore. We note that the chromophore in the 1U19 crystallographic structure<sup>17</sup> displays similar geometrical features and is significantly distorted from planarity.

We observe that the three runs differ considerably in the counterion distance ( $d_{\text{counterion}}$ ), which we define as the distance

Table 1. Relevant Geometrical Parameters (See Figure 1) and ZINDO Results for the QM/MM MD Runs<sup>b</sup>

	Rho-1	Rho-2	Rho-3
QM region	RPSB	RPSB+Glu113	RPSB+Glu113+Glu181
	average/RMSF		
$d_{\text{counterion}}$	3.23/0.10	2.77/0.11	2.77/0.11
$d_{\text{C6-N16}}$	11.20/0.17	11.19/0.13	11.24/0.18
BLA	0.051/0.020	0.059/0.020	0.057/0.021
$\phi_{\text{C5-C6-C7-C8}}$	-44.2/10.1	-50.4/10.8	-45.7/9.8
$\phi_{\text{C10-C11-C12-C13}}$	-17.6/8.8	-14.4/9.4	-11.9/9.3
ZINDO ( $S_0 \rightarrow S_1$ , eV)	2.34 <sup>a</sup> /0.10	2.41 <sup>a</sup> /0.12	2.42 <sup>a</sup> /0.13
Gaussian fit to ZINDO absorption spectrum			
$\mu$ (eV)	2.33	2.40	2.41
$\sigma$ (eV)	0.10	0.12	0.12
fwhm (eV)	0.24	0.28	0.28

<sup>a</sup>The statistical error of the average energy is 0.01 eV (see ref 84). <sup>b</sup>Trajectory averages are shown together with their root mean square fluctuations (RMSF). Distances are in Å and angles are in degrees. The BLA is defined as the difference between the averages of the single and double carbon-carbon bonds lengths and computed including the bonds between C<sub>5</sub> and C<sub>15</sub>. For the Gaussian fit to the ZINDO absorption spectrum, we show the mean ( $\mu$ ), the standard deviation ( $\sigma$ ), and full width at half maximum (FWHM). The 1U19 crystallographic structure<sup>17</sup> has the following geometrical parameters (chain A/B):  $d_{\text{counterion}} = 3.45/3.28$  Å,  $d_{\text{C6-N16}} = 11.21/11.29$  Å,  $\phi_{\text{C5-C6-C7-C8}} = -30.3/-31.9^\circ$ , and  $\phi_{\text{C10-C11-C12-C13}} = -40.8/-36.1^\circ$ .

between the nitrogen on the RPSB and the closest carboxylate oxygen on the Glu113 counterion. For the **Rho-1** run, the counterion distance is about 0.4 Å longer than for the **Rho-2** and **Rho-3** runs. There is also a difference in the BLA, which has a slightly smaller average value in the **Rho-1** run. All the QM/MM runs show the same HBN and have the same starting point so it is clear that the difference in the counterion distance lies in how the interaction between the chromophore and the counterion is described. In the **Rho-1** run, we have a quantum-classical interaction, while, in **Rho-2** and **Rho-3** runs, we have a quantum-quantum interaction. It is hard to fully judge which description leads to a more accurate counterion distance as comparison with other calculations and experiments yields a mixed message. Our classical MD simulation has an average counterion distance of 2.73 Å (with a root-mean-square fluctuation of 0.11 Å), and most other theoretical studies<sup>17,34,53,60</sup> converge to a value of about 2.7 Å. On the other hand, all rhodopsin crystallographic structures<sup>14-17</sup> have a counterion distance in the range of 3.1 Å to 3.9 Å. Fortunately, we will see below that the increased counterion distance does not seem to change the thermally averaged excitation energies. Finally, we note that the **Rho-2** and **Rho-3** runs exhibit very comparable geometrical parameters and, as shown below, ZINDO excitation energies. This indicates that is not needed to treat the charged Glu181 residue as quantum in the QM/MM MD simulations.

**4.2. ZINDO Absorption Spectra.** For each of the three QM/MM MD simulations, we extract 1500–2000 equally spaced frames from the last 10 ps of the simulations, which we use to obtain the absorption spectra at room temperature. This puts some constraints on the excited-state approach we can use, which must give reasonable results and be economical. Here, we use the semiempirical ZINDO method, which surely fulfills the criterium of being affordable. Even though ZINDO has shown a reasonable performance in benchmark studies of retinal and related polyenals<sup>105</sup> as well as rhodopsin intermediates,<sup>106</sup> we need to keep in mind that ZINDO often exhibits red-shifted excitation energies as compared to more accurate approaches.<sup>107</sup> Here, we use however the ZINDO results mainly as a guide in identifying structures which are in a representative region of phase space, namely, which give excitation energies close to the maximum of the theoretical absorption band.

The ZINDO calculations are performed on cluster models that include the RPSB and the Glu113 counterion as well as other nearby residues we find to be important for the absorption. These residues have been selected starting from a much larger cluster which includes all residues within 5 Å from the chromophore, and computing the excitation energies of all possible clusters which only differ from the original 5 Å model in one missing residue, to identify the residues which affect the ZINDO excitation energies the most. The contribution to the ZINDO spectrum of all the residues not included in the final M10 cluster (see below) is negligible (less than 0.01 eV). In Figure 4, we show the convergence of the excitation energies as the cluster size is increased from the smallest model which only included the chromophore. We note that, in the clusters, the retinal chromophore is extended to include Lys296 backbone atoms and is therefore slightly larger than the RPSB model used throughout the paper. For each cluster size, the excitation

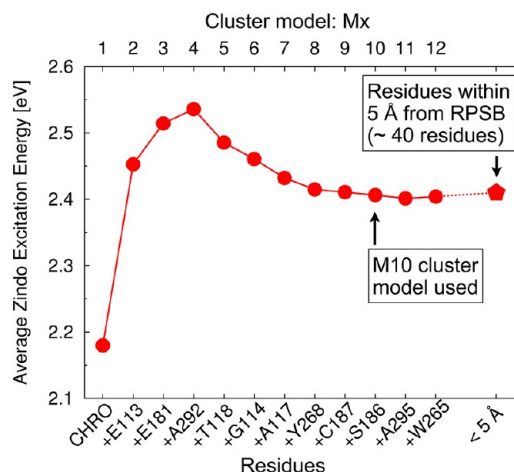


**Figure 4.** Convergence of the ZINDO average excitation energy with the size of the cluster model. The smallest cluster consists of only the chromophore (here extended to include Lys296 backbone atoms), and additional residues are then added one by one. We also consider a cluster composed of all residues within 5 Å from the chromophore (about 40 residues and 720 atoms). Note that the +E113 model also includes 7 waters located around the retinal chromophore. A set of 100 equispaced frames from the **Rho-2** run is employed.

energies are computed on a subset of 100 equispaced frames from the **Rho-2** run. For the chromophore (M1 model), we obtain an average value of 2.18 eV, and adding the Glu113 counterion plus the water molecules located around the retinal chromophore (M2 model) blue-shifts the average excitation energy to 2.45 eV. The inclusion of Glu181 and Ala292 (M4 model) gives the highest excitation energy, while, starting from the M5 model, each additional residue leads to a red-shift. The average excitation energy levels off for models M10 to M12 to a converged value of 2.40 eV. The extended model given by all residues with at least one atom within 5 Å of the chromophore (about 40 residues and 720 atoms) yields an average excitation energy of 2.41 eV, that is, equal to the values obtained for the M10 to M12 clusters. It is therefore sufficient to use the M10 cluster model for the ZINDO calculations of the excitation energies. The M10 model includes about 250 atoms and is shown in Figure 5.

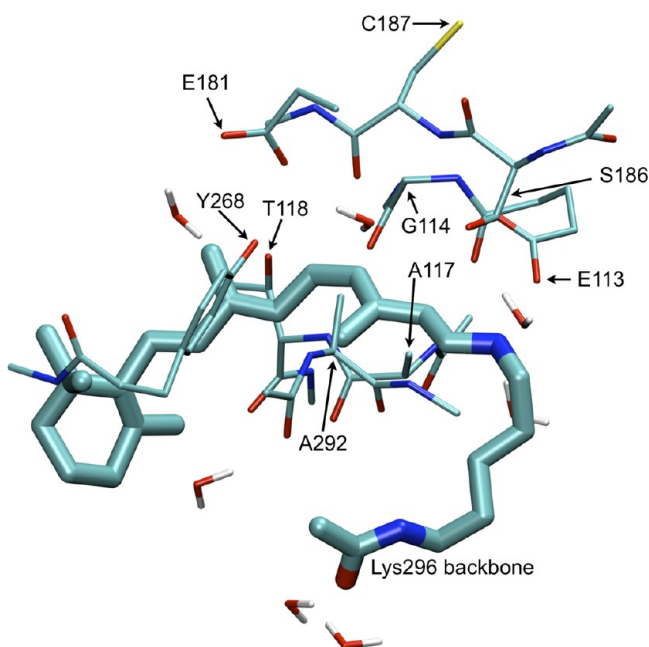


**Figure 5.** The M10 cluster model used in the ZINDO calculations, which includes about 250 atoms. For clarity, the hydrogens are not shown in the figure. See also Figures S2–S6 which show the incremental inclusion of different amino acid residues in the cluster.

With the M10 cluster, we now calculate the ZINDO absorption spectrum by weighting the excitation energy of the four lowest states with the corresponding oscillator strengths for the full set of frames. We note that the inclusion of states higher than  $S_1$  does not appreciably affect the ZINDO absorption spectrum as the higher excitations are well separated from the  $S_0 \rightarrow S_1$  excitation (see the SI). We show the spectrum for the **Rho-2** run in Figure 6. As shown in Table 1, we find that the average ZINDO excitation energies for the three runs are very similar to the absorption maxima obtained in the Gaussian fits. Furthermore, the results for the **Rho-2** and **Rho-3** runs are almost equal, which is consistent with the observation above that the inclusion of Glu181 in the QM region of the QM/MM MD simulation does not influence the structure of the protein pocket. The spectrum for the **Rho-1** run is instead slightly red-shifted by about 0.07 eV, and this shift is consistent with the slightly lower BLA. As shown below, the small differences between the

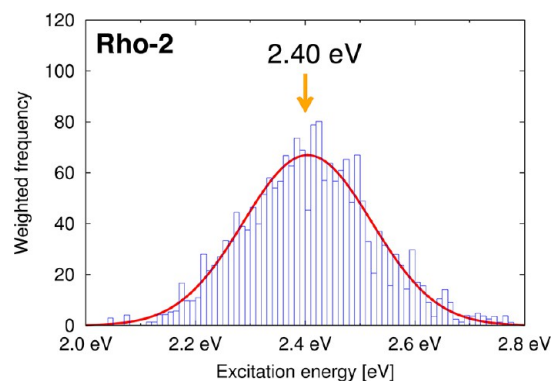


**Figure 6.** ZINDO absorption spectrum for the **Rho-2** trajectory obtained with a histogram where the excitation energies are weighted with oscillator strength (blue boxes). We show also a Gaussian fit of the histogram (red line). For the histogram, we use bins of 0.01 eV.

excitation energies computed for the **Rho-1** and the **Rho-2** or **Rho-3** trajectories are even smaller at the TDDFT level.

Finally, we observe that, for the **Rho-2** and **Rho-3** simulations, the absorption maximum of about 2.4 eV is very close to the experimental value of 2.49 eV (498 nm). Furthermore, for rhodopsin, the inhomogeneous broadening at room temperature, (i.e., the broadening of the spectrum due to thermal fluctuations in the structure) has been estimated to be 0.16 eV,<sup>26</sup> which is in good agreement with the full width at half-maximum of 0.25–0.30 eV for the ZINDO spectra.<sup>109</sup> We remark however that, since we are not considering quantum vibronic states in the ground and excited states, we can expect a difference between the location of the theoretical and experimental absorption maxima due to the neglect of nuclear quantum effects. In general, a perfect match between computed vertical energies (with classical nuclei) and experiments<sup>25–27,33</sup> might not be expected.

**4.3. TDDFT Excitation Energies.** We employ time-dependent density functional theory (TDDFT) to refine the excitation energies of frames extracted from the region of the ZINDO absorption maximum.<sup>109</sup> We select eleven frames, five from the **Rho-1**, five from the **Rho-2**, and one from the **Rho-3** run as it gives identical results as the **Rho-2** run. For these frames, we compute the TDDFT excitation energies using a quantum region that includes either the chromophore (RPSB) or the chromophore and the counterion (RPSB+Glu113), without (None) and with (Full) the MM point charges of the whole system. We also compute the excitation energies of the M10 cluster used in the ZINDO calculations.

In the TDDFT calculations, we opt to employ the CAM-B3LYP functional from the class of long-range corrected functionals since it performs well for the RPSB in the gas phase, in reproducing both highly correlated excitation energies as well as their dependence on the BLA (see SI). This must be contrasted for instance to the use of the B3LYP functional, which displays an incorrect behavior as a function of the structural model (see Table S1 and Figure S1 and also ref 46). The performance of the CAM-B3LYP functional in the presence of an MM protein will be tested against the CASPT2, NEVPT2, and QMC methods in the next section.

We show the CAM-B3LYP results in Table 2 and in Figure 7. When we include the effect of the protein environment, the frames extracted from the different QM/MM runs display rather similar excitation energies even though the counterion distance is about 0.4 Å longer for the **Rho-1** run. This is consistent with what we have observed at the ZINDO level. Given the similarity in the



**Table 2.** CAM-B3LYP/6-31+G\* Excitation Energies (eV) for Frames from the Absorption Maximum of the Rho-1, Rho-2, and Rho-3 Runs

frame	QM:	RPSB		RPSB+Glu113		M10
	MM:	none	full	none	full	none
Rho-1	1	2.49	2.68	2.71	2.69	2.58
	2	2.31	2.58	2.61	2.59	2.51
	3	2.33	2.67	2.64	2.65	2.53
	4	2.45	2.70	2.69	2.71	2.56
	5	2.38	2.69	2.67	2.70	2.57
Rho-2	6	2.36	2.64	2.71	2.66	2.60
	7	2.42	2.63	2.72	2.62	2.53
	8	2.38	2.65	2.71	2.62	2.58
	9	2.38	2.63	2.78	2.66	2.59
	10	2.38	2.68	2.78	2.70	2.62
Rho-3	11	2.36	2.65	2.72	2.65	2.61
average - Fr 1–5		2.39	2.66	2.66	2.67	2.55
average - Fr 6–11		2.38	2.65	2.74	2.65	2.59
average - Fr 1–11		2.39	2.65	2.70	2.66	2.57

excitation energies, we will not distinguish in the following between frames from individual runs. The distorted chromophore without MM charges (RPSB/None) has an average excitation energy of 2.39 eV at the CAM-B3LYP level, and, for comparison, we also compute the corresponding LC- $\omega$ PBE average value, which is equal to 2.53 eV. These average excitation energies are slightly blue-shifted with respect to the corresponding values obtained for the RPSB model optimized in the gas phase (see Table S1 in the SI). As expected, adding the full protein environment by embedding the chromophore in a sea of MM point charges (RPSB/Full) results in a blue-shift of about 0.2–0.3 eV. A larger blue-shift with respect to the gas phase (RPSB/None) is obtained if the Glu113 counterion is explicitly described quantum mechanically (RPSB+Glu113/None), and the further addition of the rest of the protein as MM charges (RPSB+Glu113/Full) brings it in agreement with the values with the smaller QM region (RPSB/Full). Therefore, the inclusion of the fixed point charges gives rise to very similar excitation energies regardless of whether the counterion is part of the QM region or not. Furthermore, in the excited states, we do not observe charge transfer between the chromophore and the counterion. Consequently, if we limit ourselves to a point-charges electrostatic embedding scheme to describe optical absorption in rhodopsin, we do not need to include the

counterion in the QM region as it seems to play a mainly electrostatic role.

If we include only RPSB or RPSB+Glu113 in the QM region with fixed point charges for the rest (RPSB/Full or RPSB+Glu113/Full), the CAM-B3LYP/MM excitation energies have an average of about 2.65 eV and are therefore blue-shifted with respect to the experimental absorption maximum of 2.49 eV. When going from this electrostatically embedded QM description to the M10 cluster model, we obtain a red-shift which ranges between 0.05 and 0.15 eV as shown in Figure 7f. One may ask if the red-shift obtained with the cluster model is due to spurious charge transfer problems, which often plague TDDFT calculations. The CAM-B3LYP functional is however from the class of long-range corrected DFT functionals designed to mend this kind of problems. In fact, we observe no indication of spurious intermolecular charge transfer, and, also for the large M10 cluster, the character of the excitation has a dominant  $\pi \rightarrow \pi^*$  contribution on the chromophore as in the calculations of the excitation energies performed using the point-charges embedding scheme. Therefore, the red-shift obtained with the cluster model is not an artifact of approximate TDDFT but is due to an enhanced description of the protein environment, resulting from the inclusion of a large number of surrounding residues in the QM region.

In Figure 7, we also present TDDFT results obtained with the LC- $\omega$ PBE functional, which is also a long-range corrected functional but has 100% exact-exchange at long-range as compared to 65% in CAM-B3LYP. As well-known for singlet excited states,<sup>110</sup> the LC- $\omega$ PBE excitation energies are blue-shifted with respect to CAM-B3LYP values but display the same trends. In particular, as shown in Figure 7f, the red-shifts obtained with the M10 cluster are very similar for LC- $\omega$ PBE and CAM-B3LYP and are also consistent with the trend observed in the ZINDO calculations, confirming the CAM-B3LYP results. The validity of the CAM-B3LYP and LC- $\omega$ PBE functionals will be further validated through a comparison with highly correlated calculations below.

In Figure 8, we show the CAM-B3LYP and LC- $\omega$ PBE excitation energies obtained for the different cluster models extracted from frames 4 and 7. As in the corresponding ZINDO study, the chromophore is here extended to include Lys296 backbone atoms and therefore slightly larger than the RPSB model used throughout the rest of the paper. Both chromophore models yield however TDDFT excitation energies which agree within 0.02 eV (both with and without the MM charges, see the

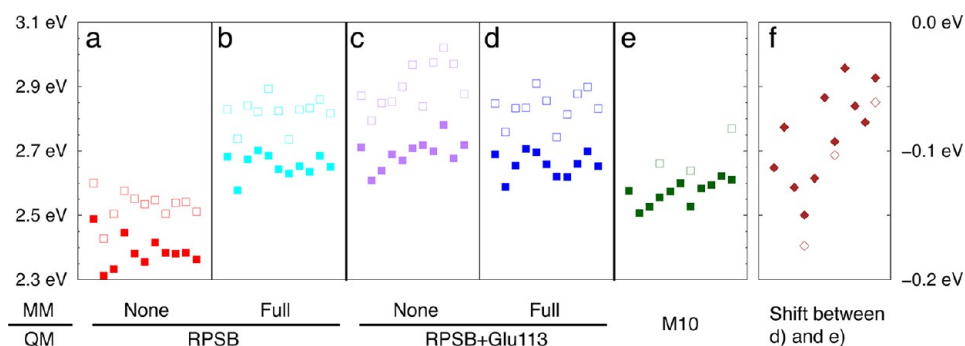


**Figure 7.** CAM-B3LYP (filled symbols) and LC- $\omega$ PBE (empty symbols) excitation energies for frames from the absorption maximum of the Rho-1, Rho-2, and Rho-3 runs. We show the excitation energies computed with different QM/MM models in panels a)–d) and with the M10 cluster in panel e). In panel f), we show the shift in the excitation energies obtained when going from RPSB+Glu113/Full to the M10 cluster. The order of the frames is the same as in Table 2.



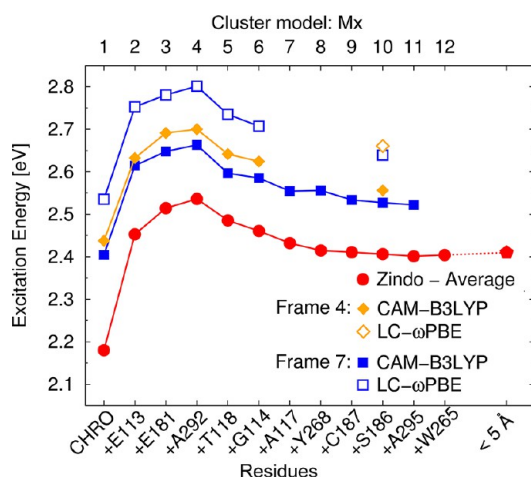


**Figure 8.** CAM-B3LYP (filled symbols) and LC- $\omega$ PBE (open symbols) excitation energies computed on different cluster models extracted from frames 4 and 7. See the caption of Figure 4 for further details.

SI). For both frames, the CAM-B3LYP excitation energies nearly parallel the average ZINDO values, being systematically blue-shifted. A similar behavior is observed for the LC- $\omega$ PBE values. Therefore, both within TDDFT and ZINDO, the negatively charged residues (Glu113 and Glu181) and Ala292 induce a blue-shift in the excitation energy while the subsequent addition of residues Thr118, Gly114, Ala117, Tyr268, Cys187, and Ser186 leads to a red-shift. The contributions of other amino acids are very small (smaller than 0.01 eV), so the TDDFT excitation energies like the ZINDO ones are converged for the M10 cluster.

In summary, our TDDFT results show that the conventional embedding scheme (a quantum chromophore only, embedded in fixed point charges) is inadequate for the computation of the optical properties of rhodopsin since it leads to excitation energies which can be blue-shifted by as much as 0.2–0.3 eV. To overcome these limitations, one needs to employ a significantly larger QM region, and we identify the M10 model as the smallest quantum model which yields converged excitation energies, in good agreement with experiments.

**4.4. Excitation Energies from Highly-Correlated Calculations.** To compute the excitation energies with various highly correlated methods, we select one frame from each trajectory: frame 4 from **Rho-1**, frame 7 from **Rho-2**, and frame 11 from **Rho-3** (see the SI for additional information). For these frames, we perform calculations with the approximate singles and doubles coupled-cluster (CC2) method, two flavors of multi-configuration perturbation theory (CASPT2) characterized by two different zero-order Hamiltonians, and the more recent  $n$ -electron valence state perturbation theory (NEVPT2). All the perturbative calculations are based on the same zero-order complete-active-space self-consistent-field (CASSCF) wave functions. Finally, we also employ the diffusion Monte Carlo (DMC) approach, which has been shown to perform well in describing excited states.<sup>66,111–115</sup> We note that we recently demonstrated that DMC, NEVPT2, and the more recent flavor of CASPT2 agree rather well for the excitation energies of the chromophore in the gas phase.<sup>66</sup> In particular, the DMC and NEVPT2 energies are in agreement within better than 0.1 eV, with CASPT2 being red-shifted with respect to NEVPT2 by at most 0.06 eV (see also Table S1).

In the CASPT2 and NEVPT2 calculations, we test the convergence of the results with respect to the size of the CAS expansion, starting from the minimal CAS(12,12) which includes all  $\pi$  electrons in the reference and a number of active orbitals equal to the number of heavy atoms as obtained by using one atomic orbital of  $p$  character per heavy atom. Since it is not generally the case that a minimal CAS space is sufficient,<sup>113,116–118</sup> the convergence of the energies must be assessed by adding more virtual orbitals to the expansion. Consequently, we also perform calculations with a CAS(12,13), a CAS(12,14), and, at the CASSCF level only, with a CAS(12,15) expansion. We find that, if we increase the active space from the minimal size to a CAS(12,13), we obtain converged CASSCF, CASPT2, and NEVPT2 excitation energies. In particular, the use of a CAS(12,13) active space leaves the CASPT2 excitation energies practically unchanged and raises the NEVPT2 values by less than 0.05 eV, bringing them in better agreement with QMC. For further information on the dependence of the perturbative calculations on the choice of active space, number of states, and single-state versus multi-state approach, we refer the reader to the SI.

The TDDFT results obtained in the previous section indicate that going beyond the conventional electrostatically embedded QM/MM description with the use of large quantum clusters changes the excitation energies by a non-negligible amount. Unfortunately, while it is possible to use large quantum models within TDDFT, a system of 250 atoms is out of reach for most highly correlated methods. Therefore, for the calculations with the high-level methods, we will remain within a point-charges embedding scheme and compare with the corresponding TDDFT/MM values in Table 3.

The CASPT2 excitation energies for the chromophore embedded in the MM charges (RPSB/Full) are very comparable to the CAM-B3LYP ones and thus blue-shifted with respect to

**Table 3. Excitation Energies (eV) on Selected Frames from the Absorption Maximum**

method	Fr.	QM:	RPSB		RPSB+Glu113		M10
		MM:	none	full	none	full	none
CAM-B3LYP <sup>a</sup>	4		2.45	2.70	2.69	2.71	2.56
	7		2.42	2.63	2.72	2.62	2.53
	11		2.36	2.65	2.72	2.65	2.61
LC- $\omega$ PBE <sup>a</sup>	4		2.57	2.82	2.85	2.83	2.66
	7		2.55	2.74	2.84	2.74	2.64
	11		2.51	2.82	2.88	2.83	2.77
CC2 <sup>b</sup>	4		2.03	2.59			
	7		2.08	2.49			
	11		2.16	2.54			
CASPT2 <sup>c</sup>	4		2.29	2.71			
	7		2.22	2.61			
	11		2.16	2.72			
NEVPT2 <sup>d</sup>	4		2.39	2.76			
	7		2.35	2.65			
	11		2.28	2.74			
DMC <sup>e</sup>	4		2.52(3)	2.78(3)			
	7			2.73(3)			
	11			2.82(3)			

<sup>a</sup>6-31+G\* basis set. <sup>b</sup>ANO-L-VDZP basis set. <sup>c</sup>SS-CASPT2 using ANO-L-VDZP and CAS(12,13) over 2 states. <sup>d</sup>NEVPT2/SC using ANO-L-VDZP and CAS(12,13) over 2 states. <sup>e</sup>DMC using D+ basis and CAS(12,12) over 2 states.

the experimental value. The behavior of the two approaches is however not the same since the CASPT2 method responds much more strongly to the addition of the MM point charges: Adding the MM point charges to the isolated chromophore (RPSB/None) results in a 0.4–0.6 eV blue-shift for CASPT2, compared to only 0.2–0.3 eV for CAM-B3LYP.

If we consider the NEVPT2 results, we observe a small difference of 0.1 eV between NEVPT2 and CASPT2 values for the isolated chromophore, and, once the MM charges are included, the two methods yield results in even better agreement, with NEVPT2 being at most 0.05 eV higher. At the NEVPT2 level, the addition of the MM point charges (RPSB/Full) results therefore in a 0.3–0.5 eV blue-shift with respect to the isolated case (RPSB/None) and a slightly less strong response to the environment than in the CASPT2 approach. We note that the NEVPT2 method is known to be sensitive to the quality of the zero-order wave function and can give an unsatisfactory performance if the correction due to dynamical correlation is large.<sup>118</sup> However, for the results presented here, this is not an issue (see the SI).

Finally, the DMC results also agree rather well with the NEVPT2 estimates and are at most 0.1 eV higher. Interestingly, DMC appears to bring the excitation energies in closer agreement with the LC- $\omega$ PBE values both for the isolated chromophore and in the MM protein. In summary, while CASPT2, NEVPT2, and DMC display larger differences (up to 0.2 eV) in the excitation energies of the isolated chromophore (RPSB/None), the three methods are significantly closer (within better than 0.1 eV) once the MM charges are added. The only approach which is at variance with the other methods is CC2, whose excitation energies of about 2.5–2.6 eV (RPSB/Full) are in fact lower and in agreement with the experimental absorption maximum at 2.49 eV, probably due to error cancellation.

The CASPT2 approach has been extensively used in the past decade to study the absorption properties of rhodopsin and other visual opsins.<sup>55–61</sup> Our results differ in the use of a more recent and improved formulation of the CASPT2 theory, which has been shown to generally give a better performance in describing electronic excitations,<sup>65,66,95,111–113,119</sup> as we will discuss in more detail below. Employing the older formulation of the CASPT2 method as used in previous rhodopsin studies results in excitation energies significantly red-shifted by 0.3 eV, in the range of 2.3–2.4 eV. A comparison of the two flavors of this perturbative approach with other methods (NEVPT2 and DMC) with their balanced description of static and dynamical correlation strongly indicates that the improved CASPT2 formulation used here is indeed more accurate.

In summary, we observe that TDDFT/CAM-B3LYP, CASPT2, NEVPT2, and DMC yield very comparable results within the conventional embedding scheme with the chromophore in the QM region and the rest of the protein treated as MM point charges. The results obtained are 0.2–0.3 eV blue-shifted as compared to the experimental absorption maximum at 2.49 eV. We stress again that, even though an enlarged quantum region brings the TDDFT energies in better agreement with the experimental value, a calculation with the same large QM region is not possible with the other methods. Nevertheless, it is plausible that a similar (or larger, given the stronger response of the high-level methods to the MM charges) red-shift in the excitation energies would be obtained for a calculation with these highly correlated methods and the same large QM cluster.

**4.5. Comparison with Previous CASPT2/MM and Other Studies.** As briefly mentioned in the previous section, the

CASPT2 approach in its older formulation has been one of the most widely used methods to investigate the optical absorption of rhodopsin<sup>55–61</sup> in the past decade. These studies have employed a conventional embedding scheme (the quantum chromophore is embedded in the point charges of the rest of the protein) and generally reported a remarkable agreement with the experimental absorption maximum, yielding results in a range of 2.3 to 2.6 eV. This must be contrasted with our findings of significantly blue-shifted excitations computed with highly correlated approaches and an MM environment. Here, we will show that the agreement of previous studies appears to be fortuitous and that the reported results depend very much on the precise details of the computational procedure employed and the ad hoc choice of the model configuration.

The older formulation of the CASPT2 approach (CASPT2/0-IPEA) is based on a different zero-order Hamiltonian than the one used in this work. The newer formulation of the CASPT2 approach (CASPT2/S-IPEA) we use employs an improved zero-order Hamiltonian, the so-called IPEA Hamiltonian, which was developed to give on average more accurate results for properties such as electronic excitations.<sup>95</sup> In our previous work on gas-phase retinal,<sup>65,66,120</sup> we have shown that CASPT2/S-IPEA gives more accurate excitation energies in agreement with NEVPT2 and DMC methods, while the CASPT2/0-IPEA excitation energies are at variance and systematically lower by 0.3 eV. The disagreement of this older CASPT2 formulation with highly correlated approaches and reference data is in line with what was reported also for other molecules.<sup>111–113,119</sup> As explained, the exact same behavior is observed in the previous section for the rhodopsin frames.

To model rhodopsin, previous CASPT2/MM studies have used the available crystallographic structures for which only the geometry of the chromophore is optimized with the CASSCF method, which largely lacks the inclusion of dynamical correlation. As we have shown for the RPSB in the gas phase, CASSCF leads to an inadequate description of the structure of retinal and yields excitation energies that are 0.3 eV higher than those obtained with more appropriate DFT structural models.<sup>65,66</sup> Another important difference with our work is that previous CASPT2/MM studies have used very different protonation states, especially, they have considered Glu181 to be protonated (neutral). While we have shown above that replacing a charged Glu181 with a neutral residue as Gln181 does not significantly affect the excitation energies, we need to keep in mind that, in our simulations, the whole protein (and not just the chromophore and selected amino acids) was thermally equilibrated for the two choices of the charge state at position 181. Finally, in previous CASPT2/MM studies, only the chromophore was included in the QM region, while the rest of the environment has been described by using Amber MM point charges, and no thermal effects were included.

To further understand the discrepancy with previous CASPT2/MM studies, we follow two routes. In the first route, we employ exactly the same structural model as used in refs 60 and 61, which was constructed from the 1U19 crystallographic structure<sup>17</sup> with an unrelaxed protein environment (the model was kindly provided by one of the authors of ref 61, N. Ferré). From this model, we also construct different structures either by changing the protonation state of Glu181 or by reoptimizing the original CASSCF chromophore with DFT and the BLYP functional. In the second route, we also start from the 1U19 crystallographic structure but use the protonation state for all residues as in our model. We then keep the protein environment

fixed and optimize the geometry of the chromophore, with either CASSCF or DFT/BLYP.

In Table 4, we present the CASPT2/MM excitation energies computed for the original structure employed in refs 60 and 61,

**Table 4. CASPT2/MM Excitation Energies (eV) Computed with the Rhodopsin (1U19) CASSCF/Amber Model Used in Refs 60 and 61<sup>a</sup>**

CASPT2	basis	excitation
0-IPEA	6-31G*	2.38
	ANO-L-VDZP	2.22
S-IPEA	6-31G*	2.75
	ANO-L-VDZP	2.63

<sup>a</sup>We note that Glu181 is protonated in this model.

with different zero-order Hamiltonians and basis sets. For the older CASPT2/0-IPEA formulation, we only obtain an excitation compatible with the experimental absorption maximum if we use the small and unconverged 6-31G\* basis set as normally done in these older studies,<sup>60,61</sup> while a better ANO-L-VDZP basis leads to a value which is too low. The CASPT2/S-IPEA formulation gives excitation energies systematically blue-shifted by about 0.4 eV. Here, we do not adopt the point of view<sup>61</sup> that certain approaches should be used in combination with particular unconverged basis sets in the study of rhodopsin but conclude that the apparent agreement of the CASPT2/0-IPEA formulation with experiments is due to a favorable, but fortuitous, cancellation of errors.

In Table 5, we consider different models constructed with different possible combinations of the protonation state of

**Table 5. CASPT2/MM Excitation Energies (eV) Obtained from Different Rhodopsin (1U19) Models<sup>b</sup>**

residue protonations	chro. opt.	Glu181	CASPT2 <sup>a</sup>
from refs 60 and 61	CASSCF	prot.	<b>2.63</b>
	CASSCF	deprot.	2.96
	BLYP	prot.	2.17
	BLYP	deprot.	<b>2.55</b>
as in this study	CASSCF	deprot.	3.14
	BLYP	deprot.	<b>2.57</b>

<sup>a</sup>CASPT2/S-IPEA with the ANO-L-VDZP basis set. <sup>b</sup>Only the chromophore is optimized with either CASSCF or BLYP, using the protonation state of Glu181 as indicated. In boldface, we indicate the excitation energies which are accidentally in close agreement with experiments.

Glu181 and methods used to optimize the chromophore. This investigation leads to the interesting finding that different models may accidentally lead to final excitation energies which are rather close. However, the corresponding structures are in fact rather different as regards the geometry of the chromophore and the chemical environment of the protein. Moreover, even though the final excitation energies from the CASSCF model from refs 60 and 61 and our BLYP model are equivalent (2.63 and 2.57 eV, respectively), the conclusions on the effect of the environment are rather different. The former model leads to a counterion quenching effect from the rest of the protein of almost 0.9 eV, while the latter is characterized by a corresponding value of only 0.1 eV (see Table S11). Clearly, these findings indicate that considering only one single structure is not a reliable procedure since the various computational ingredients (e.g., protonation

states, chromophore geometry, and excited-state method) influence significantly the excitation energies. Therefore, for one particular structure, it is easy and possible to obtain an apparent agreement with the experimental absorption maximum even though the structural model is not correct. As we have done here, the proper procedure is to validate the results with a variety of highly correlated techniques and to employ multiple representative snapshots of the chromophore–protein system obtained with thermal sampling.

Finally, we mention the recent work of ref 62, where only the chromophore is optimized within quantum Monte Carlo while keeping the rest of the protein fixed starting from one frame annealed at the PBE/MM level. This procedure results in an increased BLA of 0.088 Å and, correspondingly, an increased CAM-B3LYP/MM excitation energy of about 2.9 eV, higher than the values of 2.6–2.7 eV obtained here. The authors report an apparent agreement of the B3LYP/MM excitation energy with the experimental absorption maximum. Unfortunately, the use of the B3LYP functional for retinal systems is problematic since it gives the incorrect dependence of the excitation energies on the BLA of the chromophore. In particular, as shown in Table S1 and Figure S1, the B3LYP excitation energy decreases with increasing BLA at variance with all highly correlated approaches, while CAM-B3LYP displays the correct behavior. Therefore, the B3LYP functional cannot be used in general to study retinal configurations and the agreement with experiments obtained with the B3LYP approach on this particular frame is due to cancellations of errors. Furthermore, we note that only the chromophore is optimized within QMC at fixed protein coordinates starting from one particular frame obtained at the PBE/MM level, a procedure which, for rhodopsin, may lead to rather varying excitation energies as shown above. At last, given the consistently good agreement of CAM-B3LYP/MM with highly correlated calculations on all our frames and the similar dependence of these approaches on the BLA parameter, we might expect to obtain increased correlated excitation energies (QMC/MM, CASPT2/MM, and NEVPT2/MM) on the particular frame of ref 62, with respect to the values reported in Table 2.

## 5. DISCUSSION AND CONCLUSIONS

In this work, we have performed a thorough investigation of the absorption properties of rhodopsin with a wide range of theoretical methods. We carefully constructed a model of rhodopsin in a realistic membrane environment, which was extensively equilibrated at room temperature at the classical MD level. Starting from an unbiased initial structure selected with the help of a clustering analysis, we performed QM/MM MD simulations of more than 15 ps at room temperature to obtain an accurate geometrical description<sup>108</sup> of the retinal chromophore and of the thermal fluctuations of the chromophore–protein system. The hydrogen bond network around the chromophore was very stable throughout the classical and the QM/MM MD simulation, which is an additional indication of the robustness of our model. With the QM/MM trajectories, we have computed the ZINDO absorption spectrum of rhodopsin at room temperature, which we then used to identify configurations close to the ZINDO absorption maximum.

For these selected structures, we computed the excitation energies with a variety of first-principles approaches (TDDFT, multireference perturbation, and quantum Monte Carlo methods) in combination with different schemes to model the chromophore–protein interaction. Within the conventional



scheme of a small quantum region (the chromophore with at most the counterion) embedded in fixed, partial MM point charges, we obtained excitation energies at the TDDFT and highly correlated level that are 0.2–0.3 eV higher than the experimental absorption maximum at 2.49 eV. The use of a larger quantum region (about 250 atoms) shifts the TDDFT excitation energies to lower energies and brings them in good agreement with the experimental absorption maximum, especially considering the inherent theoretical complexity of rhodopsin. As for the many previous multireference perturbation (CASPT2) studies of rhodopsin in a classical environment,<sup>55–61</sup> claiming a remarkable agreement with experiments, we demonstrated that this agreement is fortuitous and due to a favorable cancelation of errors for the use of a superseded flavor of perturbative approach, an unconverged basis set, and an incorrect protein model. Finally, we showed that, when only one structure is used (no thermal sampling), one can often obtain the correct answer (the experimental absorption maximum) for the wrong reasons due to the arbitrariness in the choice of the many parameters (e.g., protonation states, geometry, excited-state method, embedding model, etc.) that influence the description of a system as complex as rhodopsin.

An important finding of our study is that the description of the protein in terms of classical, nonpolarizable environment as in conventional point-charges embedding schemes appears to be inadequate to describe the absorption of rhodopsin. In the past, other authors had pointed out similar caveats,<sup>45–47</sup> but these older studies were either lacking the inclusion of thermal sampling (they used only one structure for the protein) or employed a smaller range of theoretical methods to validate their conclusions. Our extensive study corroborates these older findings and strongly points to the need of adding various key active-site residues to obtain a converged and more accurate description of the optical properties of rhodopsin. Perhaps, this should not come as a surprise since the first optically allowed excitation involves a rather large transfer of positive charge from the protonated Schiff base toward the  $\beta$ -ionone ring, and a large difference in dipole moment between the ground and the excited state, estimated to be about 12 D for RPSB in solution.<sup>18</sup> Therefore, such a change upon photoexcitation should induce a response (polarization) of the protein environment, an effect not taken into account by the fixed MM point charges used in embedding schemes.

Here, we provided a better description of the environment by enlarging the quantum region to include as many as 250 atoms. Obviously, this solution is not optimal since these calculations are quite expensive already at the TDDFT level and are prohibitive for the high-level excited-state methods. However, not all hope is lost. Another important finding from our TDDFT calculations with large clusters is that the excitation energies in rhodopsin do not display intermolecular charge transfer but remain confined to the chromophore. Therefore, a multiscale partitioning of the system in an active region and a surrounding protein is still possible, and one might obtain more accurate excitation energies using a polarizable protein environment.

In conclusion, our calculations identify the necessary ingredients for an accurate description of the absorption of rhodopsin. We demonstrate the need of a realistic structural model of the system obtained through extensive QM/MM molecular dynamics simulations, which account for the thermal fluctuations in the chromophore–protein structure and ensure an accurate description of the chromophore. To estimate the absorption maximum, it is important to employ not one but

several representative configurations of the system. In addition, the use of a single structure may hide the limitations of the model, especially if this one structure happens to yield a plausible excitation energy as in many previous studies of rhodopsin. Finally, a proper description of the environment as given by a larger quantum region is crucial to accurately compute the excitation energies of rhodopsin since the minimal model used in conventional point-charges embedding schemes, where only the chromophore (and maybe the counterion) is included in the quantum region while the rest of the protein environment is described classically with a nonpolarizable force field, leads to blue-shifted excitation energies.

## ■ ASSOCIATED CONTENT

### Supporting Information

Additional computational details. Vertical excitation energies for RPSB in the gas phase. Figures of the cluster models. Bond lengths for the RPSB in the protein. ZINDO absorption spectra for all QM/MM MD simulations. Further details on the TDDFT, CASPT2, and NEVPT2 excitation energies. Coordinates for the RPSB+Glu113 QM region. This material is available free of charge via the Internet at <http://pubs.acs.org>.

## ■ AUTHOR INFORMATION

### Corresponding Author

\*E-mail: [ursula.roethlisberger@epfl.ch](mailto:ursula.roethlisberger@epfl.ch) (U.R.), [c.filippi@utwente.nl](mailto:c.filippi@utwente.nl) (C.F.).

### Notes

The authors declare no competing financial interest.

## ■ ACKNOWLEDGMENTS

The authors acknowledge Nicolas Ferré for kindly providing the rhodopsin model employed in refs 60 and 61. O.V. and C.F. acknowledge the support from the Stichting Nationale Computerfaciliteiten (NCF-NWO) for the use of the SARA supercomputer facilities and the support of the Donald Smit Center for Information Technology, University of Groningen, for the use of their Blue Gene machine. The authors also thank the CADMOS project for computer time. The financial support for CADMOS and the Blue Gene/P system is provided by the Canton of Geneva, Canton of Vaud, Hans Wilsdorf Foundation, Louis-Jeantet Foundation, University of Geneva, University of Lausanne, and Ecole Polytechnique Fédérale de Lausanne. Support from the Swiss National Science Foundation (Grant No. 200020-130082) and the NCCR-MUST interdisciplinary research program is also gratefully acknowledged.

## ■ REFERENCES

- (1) Palczewski, K. *Annu. Rev. Biochem.* **2006**, *75*, 743–767.
- (2) Smith, S. O. *Annu. Rev. Biophys.* **2010**, *39*, 309–328.
- (3) Ebrey, T.; Koutalos, Y. *Prog. Retinal Eye Res.* **2001**, *20*, 49–94.
- (4) Nickle, B.; Robinson, P. R. *Cell. Mol. Life Sci.* **2007**, *64*, 2917–2932.
- (5) Partridge, J.; De Grip, W. *Vision Res.* **1991**, *31*, 619–630.
- (6) Shichida, Y.; Imai, H. *Cell. Mol. Life Sci.* **1998**, *54*, 1299–1315.
- (7) Stenkamp, R.; Filipek, S.; Driessen, C.; Teller, D.; Palczewski, K. *Biochim. Biophys. Acta* **2002**, *1565*, 168–182.
- (8) Stenkamp, R. E.; Teller, D. C.; Palczewski, K. *Arch. Pharm. Pharm. Med. Chem.* **2005**, *338*, 209–216.
- (9) Shichida, Y.; Morizumi, T. *Photochem. Photobiol.* **2007**, *83*, 70–75.
- (10) Nielsen, M. B. *Chem. Soc. Rev.* **2009**, *38*, 913–924.
- (11) Shichida, Y.; Matsuyama, T. *Philos. Trans. R. Soc., B* **2009**, *364*, 2881–2895.
- (12) Tsutsui, K.; Shichida, Y. *Photochem. Photobiol. Sci.* **2010**, *9*, 1426–1434.

- (13) Brown, M. F.; Salgado, G. F.; Struts, A. V. *Biochim. Biophys. Acta* **2010**, 1798, 177–193.
- (14) Palczewski, K. *Science* **2000**, 289, 739–745.
- (15) Teller, D. C.; Okada, T.; Behnke, C. A.; Palczewski, K.; Stenkamp, R. E. *Biochemistry* **2001**, 40, 7761–7772.
- (16) Okada, T.; Fujiyoshi, Y.; Silow, M.; Navarro, J.; Landau, E. M.; Shichida, Y. *Proc. Natl. Acad. Sci. U.S.A.* **2002**, 99, 5982–5987.
- (17) Okada, T.; Sugihara, M.; Bondar, A.-N.; Elstner, M.; Entel, P.; Buss, V. *J. Mol. Biol.* **2004**, 342, 571–583.
- (18) Mathies, R.; Stryer, L. *Proc. Natl. Acad. Sci. U.S.A.* **1976**, 73, 2169–2173.
- (19) Fahmy, K.; Jäger, F.; Beck, M.; Zvyaga, T. A.; Sakmar, T. P.; Siebert, F. *Proc. Natl. Acad. Sci. U.S.A.* **1993**, 90, 10206–10210.
- (20) al Jandal, N.; Farrar, G. J.; Kiang, A.-S.; Humphries, M. M.; Bannon, N.; Findlay, J. B.; Humphries, P.; Kenna, P. F. *Hum. Mutat.* **1999**, 13, 75–81.
- (21) Ramon, E.; del Valle, L. J.; Garriga, P. *J. Biol. Chem.* **2002**, 278, 6427–6432.
- (22) Janz, J. M.; Farrens, D. L. *J. Biol. Chem.* **2004**, 279, 55886–55894.
- (23) Myers, A. B.; Harris, R. A.; Mathies, R. A. *J. Chem. Phys.* **1983**, 79, 603–613.
- (24) Myers, A.; Mathies, R. In *Biological Applications of Raman Spectroscopy: VOLUME 2: Resonance Raman Spectra of Polyenes and Aromatics*; Spiro, T., Ed.; John Wiley & Sons, Inc.: New York, 1987; pp 1–58.
- (25) Loppnow, G.; Mathies, R. *Biophys. J.* **1988**, 54, 35–43.
- (26) Kim, J. E.; Tauber, M. J.; Mathies, R. A. *Biophys. J.* **2003**, 84, 2492–2501.
- (27) Kamalov, V. F.; Masciangioli, T. M.; El-Sayed, M. A. *J. Chem. Phys.* **1996**, 100, 2762–2765.
- (28) Loppnow, G. R.; Mathies, R. A.; Middelndorf, T. R.; Gottfried, D. S.; Boxer, S. G. *J. Phys. Chem.* **1992**, 96, 737–745.
- (29) Lee, L.-J.; Gillie, J.; Johnson, C. K. *Chem. Phys. Lett.* **1989**, 156, 227–232.
- (30) Haacke, S.; Vinzani, S.; Schenkl, S.; Chergui, M. *ChemPhysChem* **2001**, 2, 310–315.
- (31) Yan, E. C. Y.; Kazmi, M. A.; De, S.; Chang, B. S. W.; Seibert, C.; Marin, E. P.; Mathies, R. A.; Sakmar, T. P. *Biochemistry* **2002**, 41, 3620–3627.
- (32) Sandberg, M. N.; Amora, T. L.; Ramos, L. S.; Chen, M.-H.; Knox, B. E.; Birge, R. R. *J. Am. Chem. Soc.* **2011**, 133, 2808–2811.
- (33) Birge, R. R.; Bocian, D. F.; Hubbard, L. M. *J. Am. Chem. Soc.* **1982**, 104, 1196–1207.
- (34) Röhrig, U. F.; Guidoni, L.; Rothlisberger, U. *ChemPhysChem* **2005**, 6, 1836–1847.
- (35) Sekharan, S.; Sugihara, M.; Buss, V. *Angew. Chem., Int. Ed.* **2007**, 46, 269–271.
- (36) Bravaya, K.; Bochenkova, A.; Granovsky, A.; Nemukhin, A. *J. Am. Chem. Soc.* **2007**, 129, 13035–13042.
- (37) Altun, A.; Yokoyama, S.; Morokuma, K. *J. Phys. Chem. B* **2008**, 112, 16883–16890.
- (38) Altun, A.; Yokoyama, S.; Morokuma, K. *J. Phys. Chem. B* **2008**, 112, 6814–6827.
- (39) Fujimoto, K.; Hayashi, S.; Hasegawa, J.-y.; Nakatsuji, H. *J. Chem. Theory Comput.* **2007**, 3, 605–618.
- (40) Fujimoto, K.; Hasegawa, J.-y.; Nakatsuji, H. *Bull. Chem. Soc. Jpn.* **2009**, 82, 1140–1148.
- (41) Rostov, I. V.; Amos, R. D.; Kobayashi, R.; Scalmani, G.; Frisch, M. J. *J. Phys. Chem. B* **2010**, 114, 5547–5555.
- (42) Hasegawa, J.-y.; Fujimoto, K. J.; Nakatsuji, H. *ChemPhysChem* **2011**, 12, 3106–3115.
- (43) Sekharan, S.; Morokuma, K. *J. Am. Chem. Soc.* **2011**, 133, 19052–19055.
- (44) Kaila, V. R. I.; Send, R.; Sundholm, D. *J. Phys. Chem. B* **2012**, 116, 2249–2258.
- (45) Warshel, A.; Chu, Z. T. *J. Phys. Chem. B* **2001**, 105, 9857–9871.
- (46) Wanko, M.; Hoffmann, M.; Strodel, P.; Koslowski, A.; Thiel, W.; Neese, F.; Frauenheim, T.; Elstner, M. *J. Phys. Chem. B* **2005**, 109, 3606–3615.
- (47) Houjou, H.; Inoue, Y.; Sakurai, M. *J. Phys. Chem. B* **2001**, 105, 867–879.
- (48) Matsuura, A.; Sato, H.; Houjou, H.; Saito, S.; Hayashi, T.; Sakurai, M. *J. Comput. Chem.* **2006**, 27, 1623–1630.
- (49) Watanabe, H. C.; Mori, Y.; Tada, T.; Yokoyama, S.; Yamato, T. *BIOPHYSICS* **2010**, 6, 67–78.
- (50) Rajamani, R.; Lin, Y.-L.; Gao, J. *J. Comput. Chem.* **2011**, 32, 854–865.
- (51) Hernandez-Rodriguez, E. W.; Sanchez-Garcia, E.; Crespo-Otero, R.; Montero-Alejo, A. L.; Montero, L. A.; Thiel, W. *J. Phys. Chem. B* **2012**, 116, 1060–1076.
- (52) Hoffmann, M.; Wanko, M.; Strodel, P.; König, P. H.; Frauenheim, T.; Schulten, K.; Thiel, W.; Tajkhorshid, E.; Elstner, M. *J. Am. Chem. Soc.* **2006**, 128, 10808–10818.
- (53) Frähmcke, J. S.; Wanko, M.; Phatak, P.; Mroginiski, M. A.; Elstner, M. *J. Phys. Chem. B* **2010**, 114, 11338–11352.
- (54) Frähmcke, J. S.; Wanko, M.; Elstner, M. *J. Phys. Chem. B* **2012**, 116, 3313–3321.
- (55) Ferré, N.; Olivucci, M. *J. Am. Chem. Soc.* **2003**, 125, 6868–6869.
- (56) Andruniów, T.; Ferré, N.; Olivucci, M. *Proc. Natl. Acad. Sci. U.S.A.* **2004**, 101, 17908–17913.
- (57) Coto, P. B.; Strambi, A.; Ferré, N.; Olivucci, M. *Proc. Natl. Acad. Sci. U.S.A.* **2006**, 103, 17154–17159.
- (58) Andruniów, T.; Olivucci, M. *J. Chem. Theory Comput.* **2009**, 9, 3096–3104.
- (59) Tomasello, G.; Olasso-González, G.; Altoeà, P.; Stenta, M.; Serrano-Andrés, L.; Merchaán, M.; Orlandi, G.; Bottoni, A.; Garavelli, M. *J. Am. Chem. Soc.* **2009**, 131, 5172–5186.
- (60) Strambi, A.; Coto, P. B.; Ferré, N.; Olivucci, M. *Theor. Chem. Acc.* **2007**, 118, 185–191.
- (61) Melaccio, F.; Olivucci, M.; Lindh, R.; Ferré, N. *Int. J. Quantum Chem.* **2011**, 111, 3339–3346.
- (62) Coccia, E.; Varsano, D.; Guidoni, L. *J. Chem. Theory Comput.* **2013**, 9, 8–12.
- (63) Zaari, R. R.; Wong, S. Y. *Chem. Phys. Lett.* **2009**, 469, 224–228.
- (64) Send, R.; Kaila, V. R. I.; Sundholm, D. *J. Chem. Theory Comput.* **2011**, 7, 2473–2484.
- (65) Valsson, O.; Filippi, C. *J. Phys. Chem. Lett.* **2012**, 3, 908–912.
- (66) Valsson, O.; Angeli, C.; Filippi, C. *Phys. Chem. Chem. Phys.* **2012**, 14, 11015–11020.
- (67) Gozem, S.; Huntress, M.; Schapiro, I.; Lindh, R.; Granovsky, A. A.; Angeli, C.; Olivucci, M. *J. Chem. Theory Comput.* **2012**, 8, 4069–4080.
- (68) Neri, M.; Vanni, S.; Tavernelli, I.; Rothlisberger, U. *Biochemistry* **2010**, 49, 4827–4832.
- (69) Andersson, K.; Malmqvist, P.-A.; Roos, B. O.; Sadlej, A. J.; Wolinski, K. *J. Phys. Chem.* **1990**, 94, 5483–5488.
- (70) Jorgensen, W. L.; Chandrasekhar, J.; Madura, J. D.; Impey, R. W.; Klein, M. L. *J. Chem. Phys.* **1983**, 79, 926–935.
- (71) Wang, J.; Cieplak, P.; Kollman, P. A. *J. Comput. Chem.* **2000**, 21, 1049–1074.
- (72) Röhrig, U. F.; Guidoni, L.; Rothlisberger, U. *Biochemistry* **2002**, 41, 10799–10809.
- (73) Daura, X.; Gademann, K.; Jaun, B.; Seebach, D.; van Gunsteren, W.; Mark, A. *Angew. Chem., Int. Ed.* **1999**, 38, 236–240.
- (74) Released under GPL license and freely available at the URL <http://www.cp2k.org> (accessed Sept 1, 2012).
- (75) VandeVondele, J.; Krack, M.; Mohamed, F.; Parrinello, M.; Chassaing, T.; Hutter, J. *Comput. Phys. Commun.* **2005**, 167, 103–128.
- (76) Laino, T.; Mohamed, F.; Laio, A.; Parrinello, M. *J. Chem. Theory Comput.* **2005**, 1, 1176–1184.
- (77) Laio, A.; VandeVondele, J.; Rothlisberger, U. *J. Chem. Phys.* **2002**, 116, 6941–6947.
- (78) Perdew, J. P.; Burke, K.; Ernzerhof, M. *Phys. Rev. Lett.* **1996**, 77, 3865–3868.
- (79) Schäfer, A.; Huber, C.; Ahlrichs, R. *J. Chem. Phys.* **1994**, 100, 5829–5835.
- (80) Goedecker, S.; Teter, M.; Hutter, J. *Phys. Rev. B* **1996**, 54, 1703–1710.

- (81) Hartwigsen, C.; Goedecker, S.; Hutter, J. *Phys. Rev. B* **1998**, *58*, 3641–3662.
- (82) Maseras, F.; Morokuma, K. *J. Comput. Chem.* **1995**, *16*, 1170–1179.
- (83) Bussi, G.; Donadio, D.; Parrinello, M. *J. Chem. Phys.* **2007**, *126*, 014101.
- (84) Through blocking analysis (see for instance ref 121), we estimate the excitation energy and bond lengths to be uncorrelated after about 50 fs (10 frames). We note that the averages and root-mean-square fluctuations computed with the use of all the frames are equivalent to the ones we would obtain if we only employed equidistant frames collected every 50 fs, instead of every 5 fs. In particular, given the large number of frames employed, the statistical errors on the average bond lengths and ZINDO excitation energy are in fact as small as 0.001 Å and 0.01 eV. Finally, as shown in the SI, the shape of the spectrum is unchanged if we employ 50 fs as sampling frequency to build the spectrum.
- (85) Frisch, M. J.; Trucks, G. W.; Schlegel, H. B.; Scuseria, G. E.; Robb, M. A.; Cheeseman, J. R.; Scalmani, G.; Barone, V.; Mennucci, B.; Petersson, G. A.; Nakatsuji, H.; Caricato, M.; Li, X.; Hratchian, H. P.; Izmaylov, A. F.; Bloino, J.; Zheng, G.; Sonnenberg, J. L.; Hada, M.; Ehara, M.; Toyota, K.; Fukuda, R.; Hasegawa, J.; Ishida, M.; Nakajima, T.; Honda, Y.; Kitao, O.; Nakai, H.; Vreven, T.; Montgomery, J. A., Jr.; Peralta, J. E.; Ogliaro, F.; Bearpark, M.; Heyd, J. J.; Brothers, E.; Kudin, K. N.; Staroverov, V. N.; Kobayashi, R.; Normand, J.; Raghavachari, K.; Rendell, A.; Burant, J. C.; Iyengar, S. S.; Tomasi, J.; Cossi, M.; Rega, N.; Millam, J. M.; Klene, M.; Knox, J. E.; Cross, J. B.; Bakken, V.; Adamo, C.; Jaramillo, J.; Gomperts, R.; Stratmann, R. E.; Yazyev, O.; Austin, A. J.; Cammi, R.; Pomelli, C.; Ochterski, J. W.; Martin, R. L.; Morokuma, K.; Zakrzewski, V. G.; Voth, G. A.; Salvador, P.; Dannenberg, J. J.; Dapprich, S.; Daniels, A. D.; Farkas, G.; Foresman, J. B.; Ortiz, J. V.; Cioslowski, J.; Fox, D. J. *Gaussian 09 Revision A.02*; Gaussian Inc.: Wallingford, CT, 2009.
- (86) Yanai, T.; Tew, D. P.; Handy, N. C. *Chem. Phys. Lett.* **2004**, *393*, 51–57.
- (87) Vydrov, O. A.; Heyd, J.; Krukau, A. V.; Scuseria, G. E. *J. Chem. Phys.* **2006**, *125*, 074106.
- (88) Vydrov, O. A.; Scuseria, G. E. *J. Chem. Phys.* **2006**, *125*, 234109.
- (89) TURBOMOLE V5.1 2008, a development of University of Karlsruhe and Forschungszentrum Karlsruhe GmbH, 1989–2007, TURBOMOLE GmbH, since 2007. Available from <http://www.turbomole.com> (accessed Sept 1, 2012).
- (90) Eichkorn, K.; Treutler, O.; Öhm, H.; Häser, M.; Ahlrichs, R. *Chem. Phys. Lett.* **1995**, *240*, 283–289.
- (91) Widmark, P.; Malmqvist, P.; Roos, B. O. *Theor. Chem. Acc.* **1990**, *77*, 291–306.
- (92) Dunning, T. H., Jr. *J. Chem. Phys.* **1989**, *90*, 1007–1023.
- (93) Weigend, F.; Köhn, A.; Hättig, C. *J. Chem. Phys.* **2002**, *116*, 3175–3183.
- (94) Aquilante, F.; De Vico, L.; Ferré, N.; Ghigo, G.; Malmqvist, P.-Å.; Neogrády, P.; Pedersen, T. B.; Pitoňák, M.; Reiher, M.; Roos, B. O.; Serrano-Andrés, L.; Urban, M.; Veryazov, V.; Lindh, R. *J. Comput. Chem.* **2010**, *31*, 224–247.
- (95) Ghigo, G.; Roos, B. O.; Malmqvist, P.-Å. *Chem. Phys. Lett.* **2004**, *396*, 142–149.
- (96) Forsberg, N.; Malmqvist, P.-Å. *Chem. Phys. Lett.* **1997**, *274*, 196–204.
- (97) Angeli, C.; Cimiraglia, R.; Evangelisti, S.; Leininger, T.; Malrieu, J.-P. *J. Chem. Phys.* **2001**, *114*, 10252–10264.
- (98) Angeli, C.; Cimiraglia, R.; Malrieu, J.-P. *Chem. Phys. Lett.* **2001**, *350*, 297–305.
- (99) Angeli, C.; Cimiraglia, R.; Malrieu, J.-P. *J. Chem. Phys.* **2002**, *117*, 9138–9153.
- (100) Neese, F. ORCA - an ab initio, Density Functional and Semiempirical program package, Version 2.8; Max-Planck-Institut für Bioanorganische Chemie: Mülheim an der Ruhr, 2011.
- (101) Neese, F. *WIREs Comput. Mol. Sci.* **2012**, *2*, 73–78.
- (102) CHAMP is a quantum Monte Carlo program package written by Umrigar, C. J.; Filippi, C.; and collaborators.
- (103) Burkatzki, M.; Filippi, C.; Dolg, M. *J. Chem. Phys.* **2007**, *126*, 234105.
- (104) Ferré, N.; Ángyán, J. G. *Chem. Phys. Lett.* **2002**, *356*, 331–339.
- (105) López, C. S.; Faza, O. N.; Estévez, S. L.; de Lera, A. R. *J. Comput. Chem.* **2006**, *27*, 116–123.
- (106) Campomanes, P.; Horta, B.; Neri, M.; Vanni, S.; Tavernelli, I.; Rothlisberger, U. Private communication, 2012.
- (107) Silva-Junior, M. R.; Thiel, W. *J. Chem. Theory Comput.* **2010**, *6*, 1546–1564.
- (108) A similar thermal broadening is obtained with the use of frames from the much longer classical MM trajectory. This finding further validates that the sampling time of our QM/MM simulations is sufficient to obtain a converged spectrum.
- (109) CAM-B3LYP calculations on randomly selected frames in the region of the maximum and in the tails of the ZINDO spectrum yield a rigid blue-shift of 0.2–0.3 eV in the excitation energies with respect to the ZINDO values. Therefore, the TDDFT spectrum (although shifted) roughly preserves the same shape as the ZINDO spectrum, a finding that validates the procedure of selecting frames from the region of the ZINDO absorption maximum for further analysis.
- (110) Jacquemin, D.; Wathelet, V.; Perpète, E. A.; Adamo, C. *J. Chem. Theory Comput.* **2009**, *5*, 2420–2435.
- (111) Filippi, C.; Zaccheddu, M.; Buda, F. *J. Chem. Theory Comput.* **2009**, *5*, 2074–2087.
- (112) Filippi, C.; Buda, F.; Guidoni, L.; Sinicropi, A. *J. Chem. Theory Comput.* **2012**, *8*, 112–124.
- (113) Send, R.; Valsson, O.; Filippi, C. *J. Chem. Theory Comput.* **2011**, *7*, 444–455.
- (114) Dubecký, M.; Derian, R.; Horváthová, L.; Allan, M.; Štich, I. *Phys. Chem. Chem. Phys.* **2011**, *13*, 20939–20945.
- (115) Zimmerman, P. M.; Toulouse, J.; Zhang, Z.; Musgrave, C. B.; Umrigar, C. J. *J. Chem. Phys.* **2009**, *131*, 124103.
- (116) Pastore, M.; Angeli, C.; Cimiraglia, R. *Theor. Chem. Acc.* **2007**, *118*, 35–46.
- (117) Angeli, C.; Cimiraglia, R.; Cestari, M. *Theor. Chem. Acc.* **2009**, *123*, 287–298.
- (118) Angeli, C.; Pastore, M. *J. Chem. Phys.* **2011**, *134*, 184302.
- (119) Schreiber, M.; Silva-Junior, M. R.; Sauer, S. P. A.; Thiel, W. *J. Chem. Phys.* **2008**, *128*, 134110.
- (120) Valsson, O.; Filippi, C. *J. Chem. Theory Comput.* **2010**, *6*, 1275–1292.
- (121) Flyvbjerg, H.; Petersen, H. G. *J. Chem. Phys.* **1989**, *91*, 461.